

# HERMeS Thruster Magnetic Field Topology Optimization Study: Performance, Stability, and Wear Results

IEPC-2019-902

*Presented at the 36th International Electric Propulsion Conference  
University of Vienna • Vienna, Austria  
September 15-20, 2019*

Hani Kamhawi<sup>1</sup>, Jonathan Mackey<sup>2</sup>, Jason Frieman<sup>3</sup>, Wensheng Huang<sup>4</sup>, Timothy Gray<sup>5</sup>, and Thomas Haag<sup>6</sup>  
*National Aeronautics and Space Administration Glenn Research Center, Cleveland, OH, 44135, USA*

and

Ioannis Mikellides<sup>7</sup>

*Jet Propulsion Laboratory, California Institute of Technology, Pasadena, CA, 91109, USA*

**Abstract:** NASA's Hall Effect Rocket with Magnetic Shielding (HERMeS) 12.5-kW Technology Demonstration Unit-1 (TDU-1) has been the subject of extensive technology maturation in preparation for flight system development. The TDU-1 thruster utilizes a magnetically shielded field topology and has demonstrated the elimination of the discharge channel erosion as a life-limiting mechanism. Extensive wear testing of the TDU Hall thrusters has identified the thruster front pole covers as the next life-limiting component. This effort aims to explore and investigate alternate magnetic field topologies to assess whether reductions in the front pole cover erosion can be attained while still maintaining very low erosion rates on the discharge channel walls. Four candidate magnetic field topologies that reduce the effectiveness of the shielding along the discharge channel walls with the intent to also reduce the erosion rates along the front pole covers were designed. Three of the four candidate magnetic field topologies (B1, B2, and B4) have been manufactured and were subjected to an extensive test campaign that included laser induced fluorescence (LIF), performance, stability, wear, plume, and thermal characterization. In Phase I, LIF measurements along the discharge chamber centerline found that upstream retraction of the thruster's peak magnetic field does result in an upstream shift of the acceleration zone, but the magnitude of the shift does not correspond one-to-one to the shift in the location of the peak radial magnetic field magnitude. Phase II test segment results found that at a normalized thruster magnetic field setting of 1, the thruster performance was similar for all configurations. Discharge current waveforms indicated that configurations B0, B1, and B2 have similar oscillatory profiles with the B2 configuration transitioning to a higher oscillatory mode at 400 V instead of the 450-V observed for configurations B0 and B1. Configuration B4 waveforms indicate that the thruster was operating in a very oscillatory mode above 325-V. At 12.5kW/600-V operation, the inner front pole cover erosion rates for configuration B1 were approximately 65% relative to B0, and the erosion rates for configuration B2 were 40%

---

<sup>1</sup> Senior Research Engineer, Electric Propulsion System Branch, [Hani.Kamhawi-1@nasa.gov](mailto:Hani.Kamhawi-1@nasa.gov).

<sup>2</sup> Research Engineer, Electric Propulsion System Branch, [Jonatha.a.Mackey@nasa.gov](mailto:Jonatha.a.Mackey@nasa.gov).

<sup>3</sup> Research Engineer, Electric Propulsion System Branch. [Frieman.d.Frieman@nasa.gov](mailto:Frieman.d.Frieman@nasa.gov).

<sup>4</sup> Research Engineer, Electric Propulsion System Branch. [Wensheng.Huang@nasa.gov](mailto:Wensheng.Huang@nasa.gov).

<sup>5</sup> Research Engineer, Electric Propulsion System Branch. [Timothy.g.Gray@nasa.gov](mailto:Timothy.g.Gray@nasa.gov).

<sup>6</sup> Senior Research Engineer, Electric Propulsion System Branch. [Thomas.w.Haag@nasa.gov](mailto:Thomas.w.Haag@nasa.gov).

<sup>7</sup> Principal Engineer, Electric Propulsion Group, [Ioannis.g.Mikellides@jpl.nasa.gov](mailto:Ioannis.g.Mikellides@jpl.nasa.gov).

**relative to B0. Analysis of the performance, stability, and wear test results of configurations B0, B1, B2, and B4 indicates that configuration B2 may present an alternative option for B0 because it mostly maintained the same performance and stability as configuration B0 but with 40% of B0's inner front pole cover erosion rate.**

## I. Introduction

For missions beyond low Earth orbit, spacecraft size and mass can be dominated by onboard chemical propulsion systems and propellants that may constitute more than 50% of the spacecraft mass. This impact can be substantially reduced through the utilization of Solar Electric Propulsion (SEP) due to its substantially higher specific impulse capability. Studies performed for NASA's Human Exploration and Operations Mission Directorate (HEOMD) and Science Mission Directorate have demonstrated that a 40-kW-class SEP capability can be enabling for both near term and future architectures and science missions [1].

Since 2012, NASA has been developing a 13.3-kW Hall thruster electric propulsion string that can serve as the building block for realizing a 40-kW-class SEP capability. NASA continues to evolve a human exploration approach for beyond low-Earth orbit and to do so, where practical, in a manner involving international, academic, and industry partners [2]. NASA publicly presented a reference exploration concept at the HEOMD Committee of the NASA Advisory Council meeting on March 28, 2017 [3]. This approach is based on an evolutionary human exploration architecture, expanding into the solar system with cis-lunar flight testing and validation of exploration capabilities before crewed missions beyond the earth-moon system and eventual crewed Mars missions. One of the key objectives is to achieve human exploration of Mars and beyond through the prioritization of those technologies and capabilities best suited for such a mission in accordance with the stepping stone approach to exploration [4]. NASA recently announced plans to send astronauts to the lunar surface by 2024 as part of the newly formed Artemis program. A key enabling aspect of the Artemis program is the Gateway that provides access to the lunar surface. The first element of the Gateway is the Power and Propulsion Element (PPE), illustrated in Figure 1, in which NASA recently announced a commercial partnership to develop and demonstration a high-powered SEP spacecraft with Maxar Technologies, formerly Space Systems Loral (SSL) [5]. The PPE will reach and maintain lunar orbit by incorporating two high-powered SEP strings developed by NASA, in partnership with Aerojet Rocketdyne, and Maxar [4]. The PPE is baselined to include two 13-kW Advanced Electric Propulsion System (AEPS) strings and four 6-kW Hall thrusters, currently under development by Maxar, for a total beginning-of-life propulsion power of over 60 kW [4]. High-power SEP is one of those key technologies that has been prioritized because of its significant exploration benefits. A high-power, 60-kW-class Hall thruster propulsion system provides significant capability and represents, along with flexible-blanket solar array technology, a readily scalable technology with a clear path to much higher power systems [6].

The 13.3-kW Hall thruster system development, led by the NASA Glenn Research Center (GRC) and the Jet Propulsion Laboratory (JPL), began with maturation of the high-power Hall thruster and power processing unit. The technology development work has transitioned to Aerojet Rocketdyne (AR) via a competitive procurement selection for the Advanced Electric Propulsion System (AEPS) contract. The AEPS contract includes the development, qualification, and multiple flight 1-kW electric propulsion string deliveries [7, 8]. The AEPS Electric Propulsion (EP) string consists of the Hall thruster, power processing unit (including digital control and interface functionality), xenon flow controller, and associated intra-string harnesses. NASA continues to support the AEPS development leveraging in-house expertise, plasma modeling capability, and world-class test facilities. NASA also executes AEPS and mission risk reduction activities to support the AEPS development and mission application [9, 10].

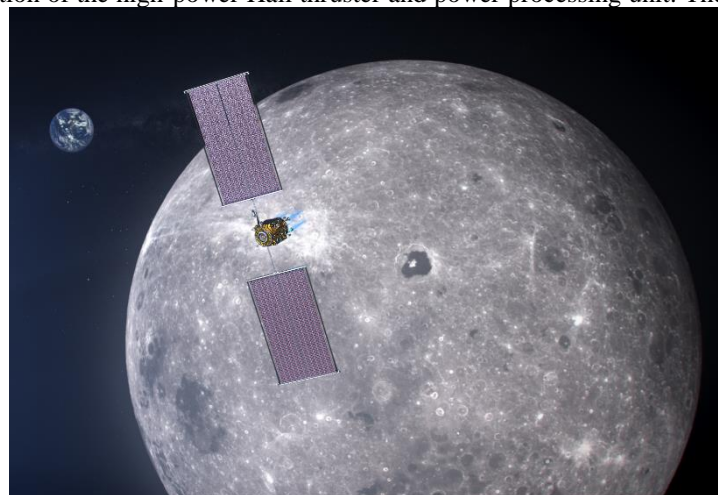


**Figure 1. NASA concept of the Power Propulsion Element [Credits: NASA].**

This paper is organized as follows: in Section II a summary of the HERMeS thruster's test campaign at NASA GRC is presented; in Section III the motivation for this effort is presented; in Section IV a summary of the magnetic field topologies' design, Hall2De modeling, and Phase I test results is presented; in Section V results from the most current test campaign (Phase II) are presented; in Section VI a discussion of the Phase II results is presented; and in Section VII the paper summary, conclusions, and future work are presented.

## II. Background

NASA's Hall Effect Rocket with Magnetic Shielding (HERMeS) 12.5-kW TDU-1 has been the subject of extensive technology maturation in preparation for flight system development starting in 2014. [11, 12, 13, 14, 15] A number of tests were performed on the thruster, and the results of these tests were presented in 2016. [16, 17, 18, 19, 20, 21] The tests assessed the performance, stability, facility effects, and thermal operation of the HERMeS thruster.

A graphite front pole cover thruster configuration with the thruster body electrically tied to cathode was selected as the baseline configuration [16, 17]. Performance characterization tests found that higher thruster performance was attained with the graphite front pole cover configuration and the thruster electrically tied to cathode. A total thrust efficiency of 68% and a total specific impulse of 2,820-sec were demonstrated at a discharge voltage of 600-V and a discharge power of 12.5-kW. Thruster stability regimes were characterized with respect to the thruster discharge current oscillations (discharge current peak-to-peak (p2p) and root-mean-square (RMS) magnitudes), along with maps of the current-voltage-magnetic field (IVB). Background pressure variation characterization tests were performed over a range of pressures from 4.6 to  $\sim 26 \mu\text{Torr-Xe}$  [16]. Finally, the IVB maps of the TDU-1 thruster indicated the thruster operation became more oscillatory at discharge voltages of  $\sim 450\text{-V}$  and that the thruster transitioned to a more oscillatory mode at 500-V and 600-V as can be seen in Fig. 2 [16, 22]. Detailed plume characterization of the TDU-1 and TDU-3 thrusters was performed [18, 22].

Results from the plume characterization results found that TDU-1 and TDU-3 plume profiles had an almost identical profiles. Figure 3 presents the ion energy per charge profiles for TDU-1 during Vacuum Facility 5 (VF-5) testing at NASA GRC. Results in Fig. 3 are presented for 300-V, 9.4-kW and 400-V, 12.5-kW operations. Both profiles show that primary ions were detected at the  $90^\circ$  polar angle. This is critical because, if of sufficient flux, these primary ions can erode spacecraft surfaces

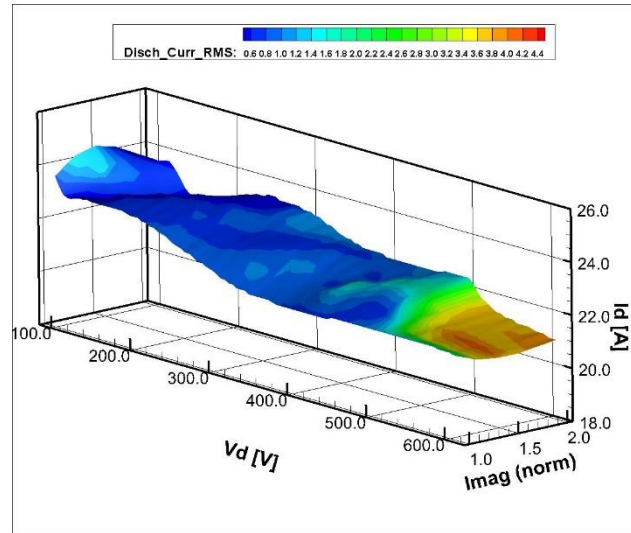


**Figure 2. VF-5 TDU-3 IVB map of discharge current RMS at 20.6-mg/s at a cathode flow fraction of 7% for discharge voltages of 100-V to 610-V and normalized magnetic field strengths of 1**

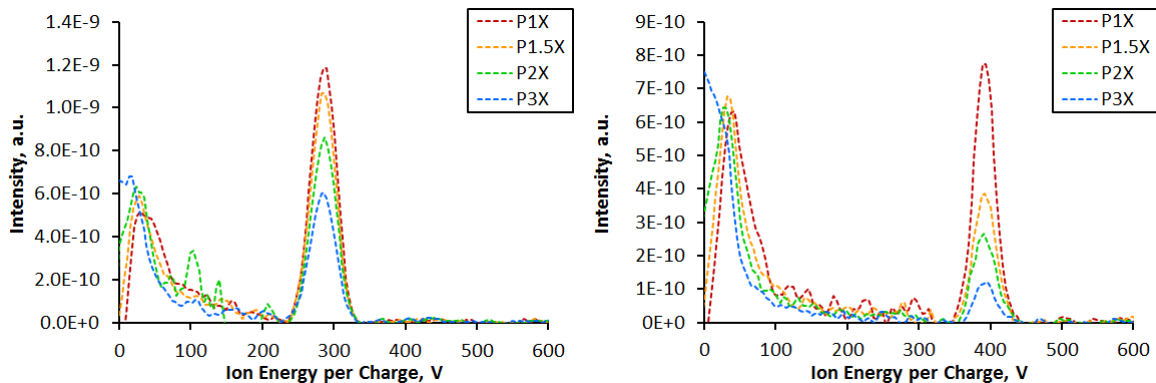


**Figure 3. TDU-1 thruster ion energy per charge profiles at various background pressures for the 300-V, 9.4-kW (left) and 400-V, 12.5-kW (right) throttle points at a polar angle of  $90^\circ$ . [18]**

causing them to degrade over the mission duration. The presence of these energetic primary ions at large plume angles can potentially complicate EP system integration on the spacecraft.

The wear characteristics of the HERMeS thruster has been explored in a series of test campaigns and detailed modeling efforts. The key components that were monitored during the wear test campaigns were the discharge channel surfaces, front pole cover surfaces, keeper downstream surface, and cathode and keeper orifices. TDU-1 and TDU-3 wear testing found that measurable erosion of the inner front pole cover was occurring, but the erosion rates were low enough to meet the thruster life plus margin requirement of greater than 23-khours [23, 24, 25]. Figures 4 and 5 present front pole cover erosion results from the TDU-3 wear test at low background pressure. Results in Figs. 4 and 5 indicate that the inner and outer front pole covers are eroding with a peak erosion rate of 120- $\mu\text{m}/\text{hr}$  and 80- $\mu\text{m}/\text{hr}$ , respectively, at the 300-V, 6.25-kW operating condition [25].

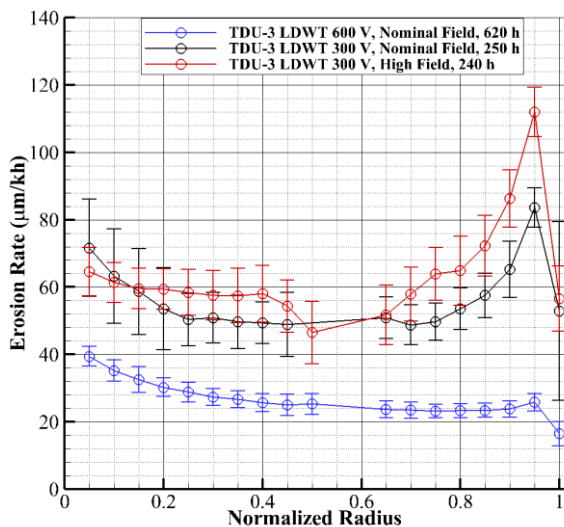


**Figure 4: Inner front pole cover erosion rates from the TDU-3 wear test.[24]**

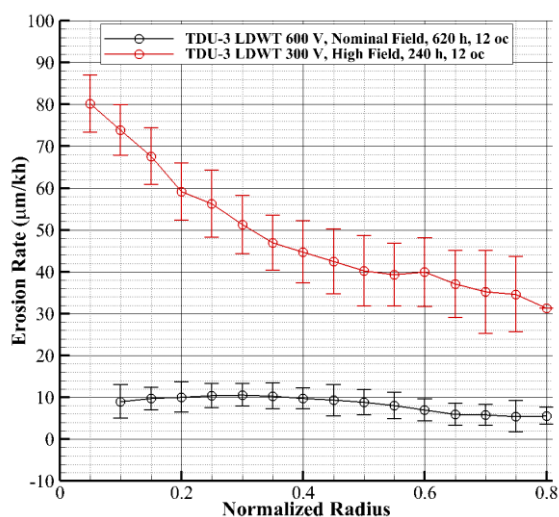


**Figure 5: Outer front pole cover erosion rates from the TDU-3 wear test.[24]**

### III. Motivation

During the design phase of the HERMeS thruster, the approach was to design a magnetic circuit that leveraged the lessons learned from the BPT-4000, NASA-300MS, and the H6MS thruster work [26, 27, 28]. The TDU-1 magnetic field topology was sufficiently shielded to assure that discharge channel erosion was eliminated. This was validated by the plasma wall probe test and wear tests that indicated no measureable erosion on the discharge channel [29]. During the plasma wall probe test campaign, anode potentials were measured at the downstream chamfer edge of the discharge channel, this indicated that the thruster was magnetically shielded. However, while the HERMeS TDU-1 and TDU-3 wear test campaigns found that discharge channel erosion rates were undetectable, erosion of the front pole covers was observed at measureable levels with sputter-resistant material, thus rendering the front pole covers as the next life-limiting mechanism. The HERMeS thruster magnetic field topology optimization effort aims to strike a balance where the front pole cover erosion is reduced at the expense of increased discharge channel erosion rates while still maintaining the thruster's capability to exceed its propellant throughput capability.

The objectives of the HERMeS thruster magnetic field topology characterization and optimization tests were to evaluate at least three new candidate magnetic field topologies. The experimental effort, supported by a detailed modeling effort, aims to determine if any of the new candidate topologies can:

- Reduce the front pole cover erosion rates from the levels being currently measured (Figs 4 and 5). The new candidate magnetic field topologies are designed to reduce the front pole cover erosion rates while still maintaining low discharge channel erosion rates consistent with the required mission(s) propellant throughput capability;
- Reduce the plume divergence of the HERMeS thruster and reduce the high-energy ion population that have been detected at large plume angles. This will avail to the spacecraft designers more options for the placement of the Hall thrusters on the spacecraft;

- Improve the stability of the HERMeS thruster by reducing the oscillation levels during thruster operation particularly above 450-V. This effort will help elucidate whether any of the new candidate magnetic field topologies can impact when the transition to a high oscillatory mode occurs, whether the thruster still transitions to a high oscillatory mode, and whether the magnitude of the oscillations can be reduced; and
- Reduce the magnetic circuit components' saturation at high magnetic field settings which would permit the attainment of even higher magnetic field magnitudes while still maintaining the desired magnetic field topology.

#### IV. Magnetic Optimization Design, Modeling, and Phase I Test Campaign Results Summary

To perform the magnetic field topology optimization study, NASA GRC and JPL initiated a task to evaluate candidate topologies. Table 1 lists the magnetic optimization design and test campaign activities. NASA GRC designed four new magnetic field topologies that were then modeled by JPL's Hall2De code. The new topologies present the first step in investigating new options for the HERMeS thruster magnetic field topology. [28, 30, 31] Details of the new magnetic field topologies' design and the preliminary modeling effort using the Hall2De code were reported last year at the 2018 AIAA Joint Propulsion Conference [32].

**Table 1: Listing of magnetic optimization design and test campaign effort. B00 is the baseline magnetically shielded TDU-1 magnetic field topology**

Test Phase	Test Description	Thruster Configuration
	Design new magnetic field topologies	B1,B2,B3,B4
	Hall2De modeling of new topologies	B1,B2,B3,B4
	Fabricate new magnetic circuit components	B1,B2,B4
	Map new TDU-1 magnetic topologies	B1,B2,B4
I	Thruster Bakeout Laser Induced Fluorescence (LIF) Magnetic Mapping Oscillations Characterization	B0,B4,B2,B1 (order of testing)
II	Thruster Bakeout Performance Plume Thermal IVBs Cathode flow fraction (CFF) Optical emission spectroscopy (OES) Wear (600 V, 12.5 kW, nominal field)	B2,B1,B0,B4 (no wear) (order of testing)

To design the new magnetic field topologies, a commercial magnetic field solver was used. Four magnetic field topologies were designed (B1-B4). Modeling using the Hall2De code was then performed. All four new topologies were then used to construct their respective magnetic field aligned meshes (MFAMs) in Hall2De, and new simulations were performed to assess discharge channel erosion. Hall2De modeling results (shown in Figure 6) found that for all four candidate topologies, the discharge channel erosion rates are higher than B0, with increasing values occurring further upstream from the channel exit along the chamfer. Similar results are found for the outer wall. Though the erosion rates increase relative to B0, it is noted that the highest values observed in B4 remain approximately two orders of magnitude below those observed in the H6US [28]. Moreover, at the maximum value of ~100- $\mu\text{m}/\text{kh}$  (B4) and assuming that this value does not change as material is lost during thruster operation, it would take approximately 38-khr for the channel to be completely eroded. For reference, the specification for the HERMeS thruster calls for 23 khr of operation of the propulsion system that must be demonstrated with a 50% margin (resulting in 34.5-khr). Thus, even the worst magnetic field topology assessed in this investigation (B4) meets the HERMeS propellant throughput requirement. The impact on the front pole cover erosion based on the current simulations is still under investigation since part of the physics that drive erosion along these boundaries remains elusive. Nevertheless, the evidence from previous wear test results, not only of the HERMeS thruster but also those comparing pole erosion in magnetically

shielded and unshielded versions of the same thruster (e.g., H6US vs. H6MS) suggest that pole erosion is expected to decrease as the magnetic field, and naturally the acceleration region, are retracted.

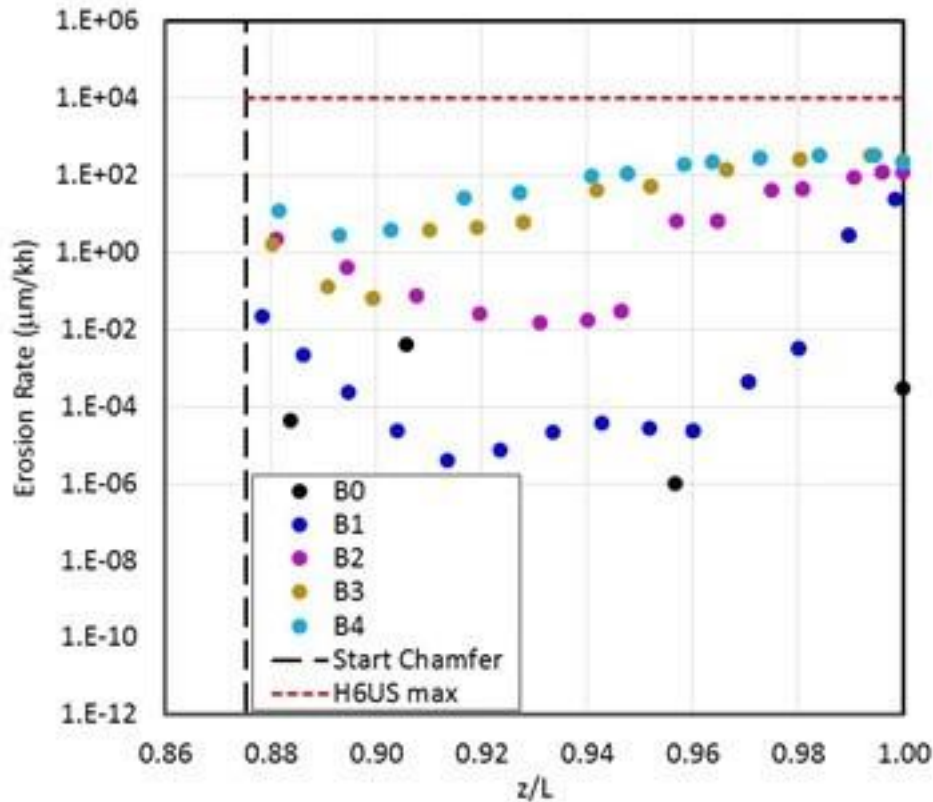


**Figure 6. Computed erosion rates along the inner channel wall of HERMeS for MS topologies B1-B4. Also shown for reference is the maximum rate measured in the 6-kW H6US. The chamfered region of the wall begins at  $z/L=0.875$ .**

Three of the four configurations that were designed were fabricated for the TDU-1 thruster magnetic circuit. The configuration B3 was designed and assessed in the model but never built, since it could have been fabricated if test results from the other three configurations indicated that the B3 configuration was needed. The three magnetic circuit configurations were installed into the TDU-1 thruster, and the magnetic field topologies were mapped.

Figures 7 and 8 present the measured radial magnetic field profile along the discharge channel centerline for the four magnetic field topologies. These topologies include the baseline topology B0 and the three new topologies (B1, B2, and B4). Results in Figs. 7 and 8 confirm that the peak radial magnetic field moves upstream towards the thruster anode as we progress from the B0 to B4 (Fig. 7). This is accompanied by an increase of 25% in the radial magnetic field strength at the anode face as is shown in Fig. 8.

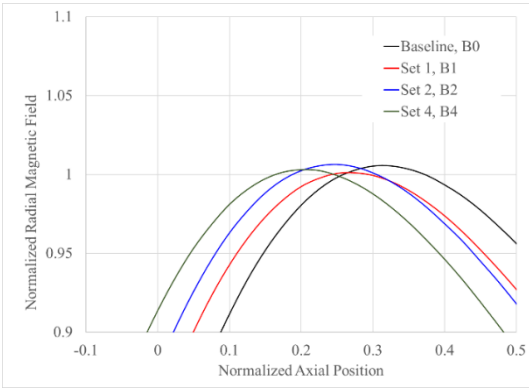


**Figure 7. Closeup of the normalized  $B_r$  magnitudes at the nominal magnetic field setting.**

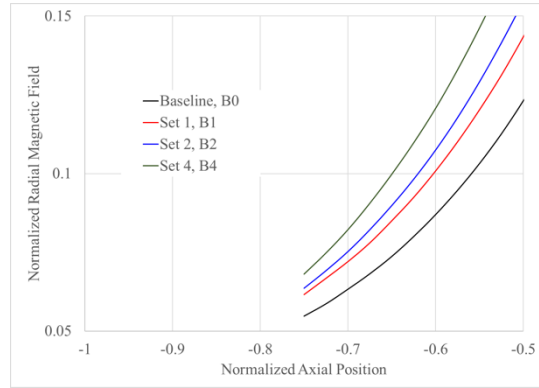


**Figure 8. Closeup of the normalized  $B_r$  magnitudes inside the discharge channel near the anode face.**

During Phase I, LIF tests were completed on the four magnetic field topologies (B0, B1, B2, and B4) [33]. Figures 9 and 10 show the discharge channel ion velocity profiles at centerline for the 300-V/6.25-kW and 600-V/12.5-kW thruster operating conditions, respectively. For 300-V operation, the B1 configuration shifts the acceleration zone slightly upstream when compared to the baseline configuration. The B2 and B4 configurations extend the acceleration zone upstream by 6 and 7 times as much as B1, respectively. For 600-V operation, both B2 and B4 configurations extend the acceleration zone upstream by about 4 times as much as B1 relative to the baseline configuration. A companion paper detailing the variation in ion acceleration characteristics during this study will be presented during the 36<sup>th</sup> International Electric Propulsion Conference. [34].

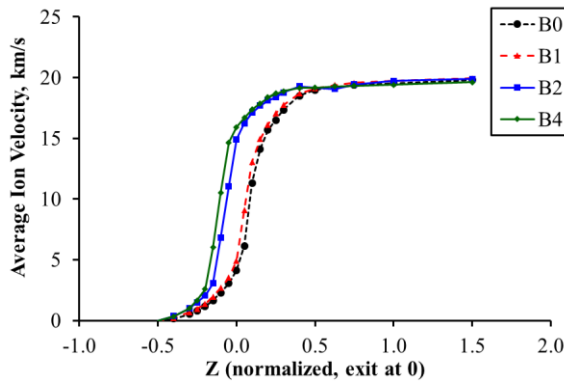


**Figure 9: Average ion velocity along the discharge channel centerline for thruster operation at 300 V and 6.25 kW for magnetic field topologies B0, B1, B2, and B4.**

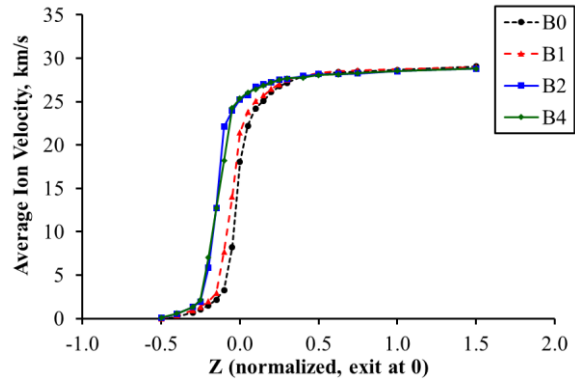


**Figure 10: Average ion velocity along the discharge channel centerline for thruster operation at 600 V and 12.5 kW for magnetic field topologies B0, B1, B2, and B4.**

## V. Phase II Test Results

After completing Phase I tests, the thruster was removed from the LIF test stand, and the thruster underwent detailed surface mapping using a commercially available profilometer [25] and was then mounted on the Vacuum Facility 6 (VF-6) thrust stand (shown in Figure 11). During the transition from the Phase I to the Phase II test campaign, the optical emission spectroscopy (OES) optics and associated linear stages were installed and aligned, and the VF-6 plasma diagnostics suite was realigned and checked out.

During the Phase II tests, configurations B0, B1, B2, and B4 were tested. For each configuration, performance was measured during all test sequences including magnet maps. Optical emission spectroscopy (OES) measurements were performed to elucidate how the discharge channel and front pole cover erosion is changing due to implementation of various magnetic field configurations [35]. Additionally, plasma plume measurements were performed using the VF-6 plasma probe suite. Measurements were performed using the Langmuir, retarding potential analyzer, Wien filter ( $E \times B$ ), and Faraday probes at various distances from the thruster [18]. Finally, a short-duration wear test was performed for B0, B1, and B2 magnetic field topologies for the thruster operating condition of 12.5-kW at 600-V discharge voltage. The sections below summarize the results from the performance, stability, and wear test results. Plume, cathode flow fraction (CFF), and thermal characterization results are still being analyzed and will be presented in a future publication.

### a. Experimental Apparatus

Testing of the HERMeS TDU-1 thruster was performed in VF-6 at NASA GRC [36, 37]. The VF-6 main chamber is 7.6 m in diameter and 18.3 m long; it is evacuated with 12 internal nude cryo pumps. For the test campaign discussed in this paper, the TDU-1 Hall thruster is located in the main volume of the chamber. Facility pressure was monitored with two xenon-calibrated Stabil ion gauges. The power supplies, data acquisition, and propellant flow system have been previously used and are described in detail in Ref. 37. The design of HERMeS TDU-1 incorporates technologies developed by NASA over nearly two decades. The thruster, along with its derivatives TDU-2 and TDU-3, incorporates a magnetic shielding topology to eliminate discharge channel erosion as a life-limiting mechanism [38, 39, 40]. The result is a significant increase in the operational lifetime, with HERMeS being designed to operate at 3,000-sec specific impulse and a projected life of >50-khours. The TDU-3 thruster maintained key design features of the TDU-1 thruster, which include: magnetic field topology, propellant manifold design, and discharge channel dimensions. The key difference between the TDU-1 and TDU-3 thruster was the grade of the discharge channel BN material; for TDU-1, it is heritage BN whereas silica composite BN is used in TDU-3. Figure 11 shows a photograph of the 12.5-kW HERMeS TDU-1 thruster installed inside NASA GRC VF-6. The performance of the TDU-1 Hall thruster was measured with an inverted pendulum null-type thrust stand. The NASA GRC high-power thrust stand has an accuracy of  $\leq 1\%$  based on a statistical analysis of the calibration and thrust zero data taken throughout the test campaign. The operation and theory of the inverted pendulum null-type thrust stand are described in detail in Refs. 41 and 42.

### b. Performance Characterization

The TDU-1 thruster was operated with magnetic field topologies B0, B1, B2, and B4. The order of testing is shown in Table 1. The measured thrust during performance characterization was corrected for thermal drift and was also power corrected to the nominal operating condition. Additionally, prior to performance characterization, thruster bakeout was performed in accordance with the HERMeS TDU procedures. Results in this section are presented for the 300-V/6.25-kW and 600-V/12.5-kW thruster operation in Figures 12 and 13, respectively. The results for thruster operation at 400-V/8.33-kW and 500-V/10.4-kW are presented in Appendix A (Figures 21 and 22, respectively).

Figures 12a-d present the performance results for the 300-V/6.25-kW thruster operating condition. Figure 12a presents the thrust magnitudes as a function of the normalized magnetic field. Results show that within the uncertainty of the measurements, configurations B0, B2, and B4 had similar thrust and configuration B1 had slightly lower thrust. Configuration B1's thrust at a normalized field strength of 1.25 is almost 25-mN lower than the other configurations at that field setting. Figure 12b presents the ratio of the discharge current to the anode flow rate ( $I/m_a$ ) as a function of the normalized magnetic field. Results show that for most of the operating conditions, configuration B0 and B1 required the least anode flow to achieve the target discharge current of 20.8-A. Results presented in Figures 12a and

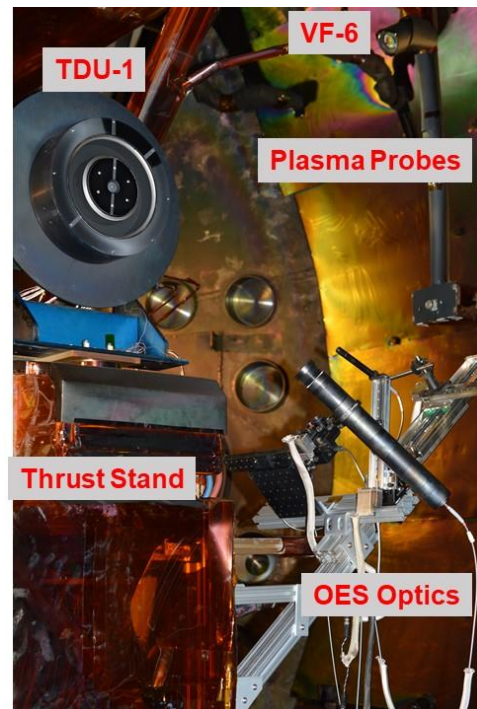


**Figure 11. TDU-1 mounted on the VF-6 thrust stand. Also shown are the plasma probes array and the OES optics.**

12b were then used to compute the total thrust efficiency (hereafter referred to as thrust efficiency) and the total specific impulse (hereafter referred to as specific impulse). Figure 12c shows that the thrust efficiencies for configurations B0, B2, and B4 are almost identical within the experimental uncertainty; the thrust efficiency of configuration B1 is lower with the difference becoming much greater at a normalized field setting of 1.25. Figure 12d shows that the specific impulse for configuration B0 is the highest (mainly due to its  $I_d/m_a$ ) with an average of  $\sim 2,020$ -sec, whereas configurations B1, B2, and B4 have an average total specific impulse of approximately 1,955-sec, 1,967-sec, and 1,960-sec, respectively.

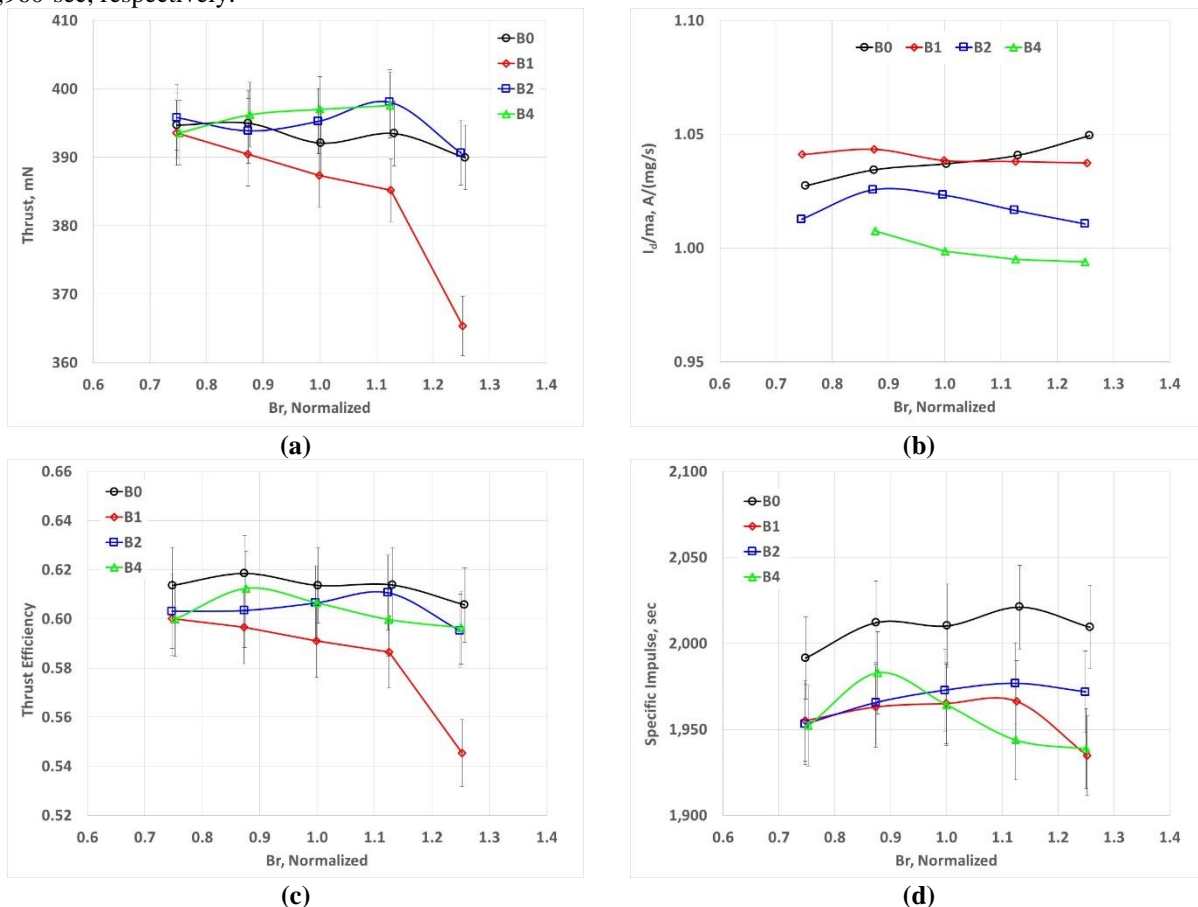


**Figure 12 a-d. Trends of thrust,  $I_d/m_a$ , thrust efficiency, and specific impulse variation with normalized magnetic field setting for configurations B0, B1, B2, and B4 for the thruster operation at 6.25-kW and 300-V discharge voltage.**

Figures 13a-d present the performance results for the 600-V/12.5-kW thruster operating condition. Figure 13a presents the thrust magnitudes as a function of the normalized magnetic field. Results show that within the uncertainty of the measurements, configurations B0 and B2 have similar thrust and configurations B1 and B4 have slightly lower thrust. Additionally, B4's thrust at a normalized field strength of 1.25 is almost 2-mN lower than configuration B0's thrust at a normalized field setting of 1.25. Figure 13b presents the  $I_d/m_a$  as a function of the normalized magnetic field. Results show that for most of the normalized field settings, configurations B0 and B1 required less anode flow to achieve the target discharge current of 20.8-A; configurations B2 and B4's discharge current to anode flow ratio was slightly lower than B0 and B1's. Results presented in Figures 13a and 13b were then used to compute the thruster's thrust efficiency and the total specific impulse. Figure 13c shows that the thrust efficiency for configurations B0, B1, and B2 is almost identical with increasing thrust efficiency as the normalized field strength is increased, while configuration B4 shows lower thrust efficiency and decreasing thrust efficiency as the normalized field strength is increased. Figure 13d shows that the total specific impulse for configuration B0 is the highest (mainly due to its  $I_d/m_a$ ) with an average of  $\sim 2,900$ -sec, whereas, configurations B1, B2, and B4 had an average specific impulse of approximately 2,830-sec, 2,820-sec, and 2,730-sec, respectively.

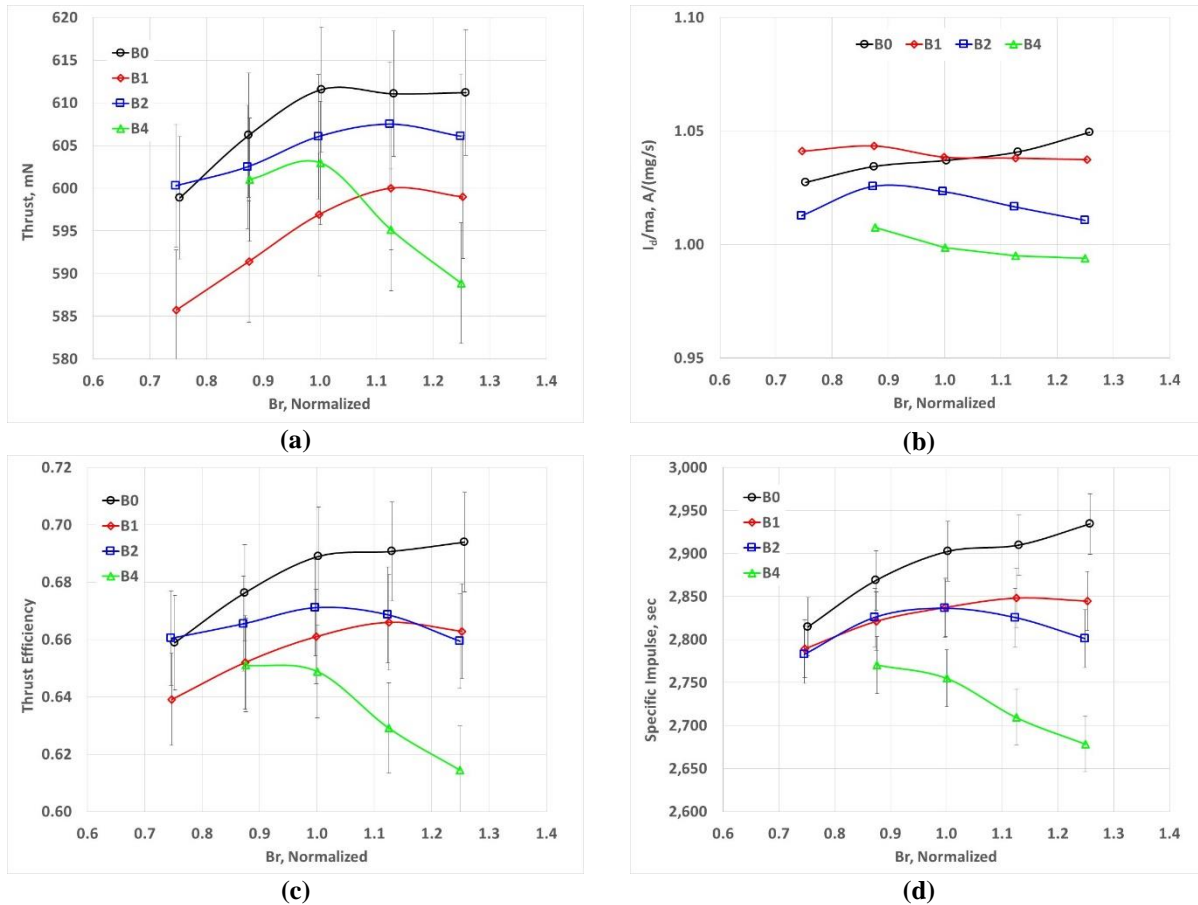
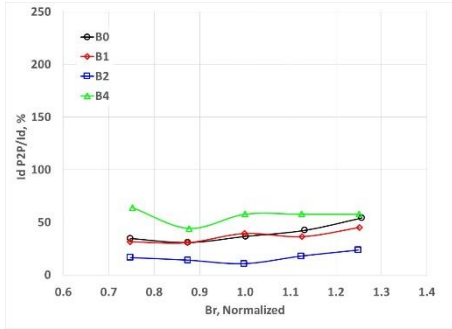


**Figure 13 a-d. Trends of thrust,  $I_d/ma$ , thrust efficiency, and specific impulse variation with normalized magnetic field setting for configurations B0, B1, B2, and B4 for the thruster operation at 12.5 kW and 600-V discharge voltage.**

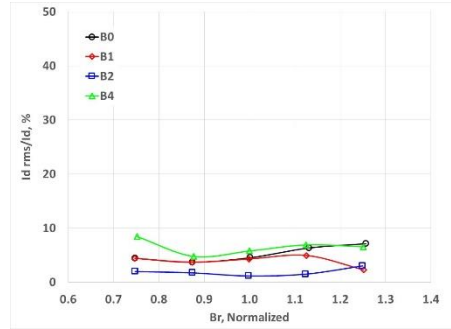
### c. Stability Characterization

To assess the stability of the TDU-1 thruster operation at the various normalized field settings, the discharge current waveform ripple was analyzed. The discharge current waveform was analyzed to determine the peak-to-peak (p2p) and root-mean-square (RMS) magnitudes of the discharge current waveform. The discharge current p2p and RMS were then used to assess the oscillation levels and stability of the thruster. In addition, current-voltage-magnetic field (IVB) maps were performed for each thruster configuration to provide insights into the global thruster stability map.

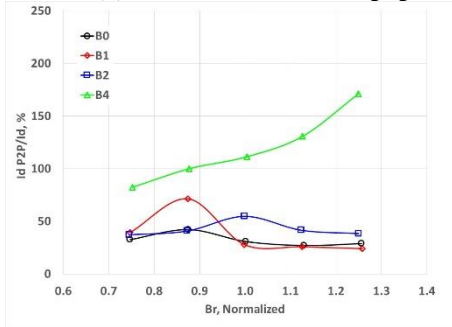
Figures 14a and 14b show that the thruster was operating in a quiescent mode at a discharge voltage of 300-V. At this discharge voltage, the discharge current oscillations levels were low for all the configurations, with the B2 configuration having the lowest level. Figures 14c and 14d, show that at a discharge voltage of 400-V, the oscillation levels for configuration B4 grew substantially. The two figures also show that configuration B2's oscillation levels were generally higher than that of configurations B0 and B1, indicating that configuration B2 was starting to transition to a higher oscillatory mode. Figures 14e and 14f, again show that configuration B4 was in a very oscillatory mode and that configuration B2's oscillations were slightly higher than those of configuration B0. At a discharge voltage of 600-V, Figures 14g and 14h show that configuration B2 had the lowest oscillation levels (almost 50% of configuration B0) and that configuration B4's oscillation levels grew higher than at 500-V operation.



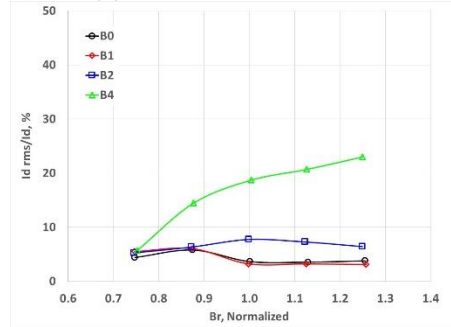
(a) 300V normalized  $I_d$  p2p



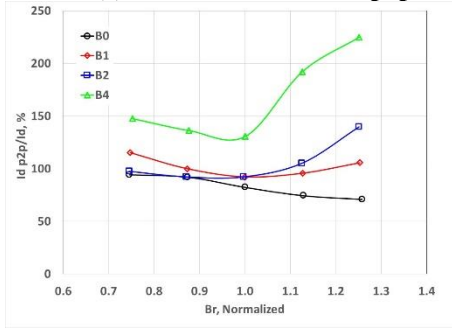
(b) 300V normalized  $I_d$  RMS



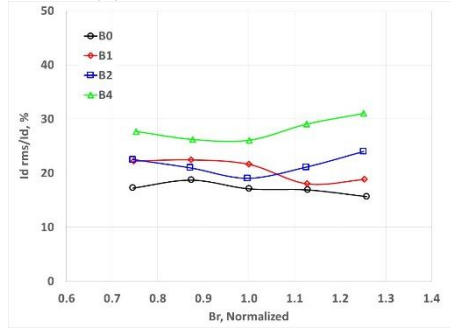
(c) 400V normalized  $I_d$  p2p



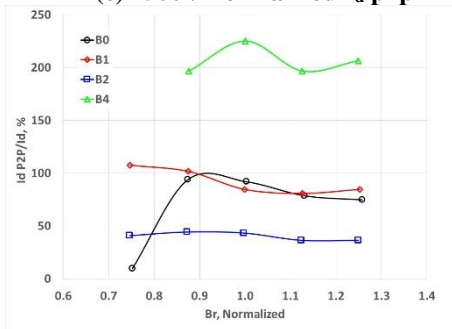
(d) 400V normalized  $I_d$  RMS



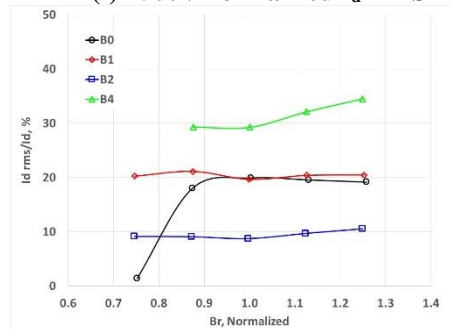
(e) 500V normalized  $I_d$  p2p



(f) 500V normalized  $I_d$  RMS



(g) 600V normalized  $I_d$  p2p



(h) 600V normalized  $I_d$  RMS

Figure 14. Discharge current normalized p2p and RMS magnitudes for thruster operation at 300-V, 400-V, 500-V, 600 V for configurations B0, B1, B2, and B4 as a function of the normalized magnetic field setting.

Figures 15a-d show the discharge current power spectral density (PSDs) for the thruster operating at discharge of 300-V, 400-V, 500-V and 600-V, respectively, at the normalized magnetic field setting of 1. The profiles shown in Figures 15a-d show that configuration B4 is the most oscillatory configuration; they also show that configuration B2 has higher oscillation levels at 400-V than configurations B0 and B1 (more energy under the curve). At discharge voltages of 500-V and 600-V and a normalized magnetic field setting of 1, the thruster operation for configuration B2 exhibits the lowest oscillation levels.

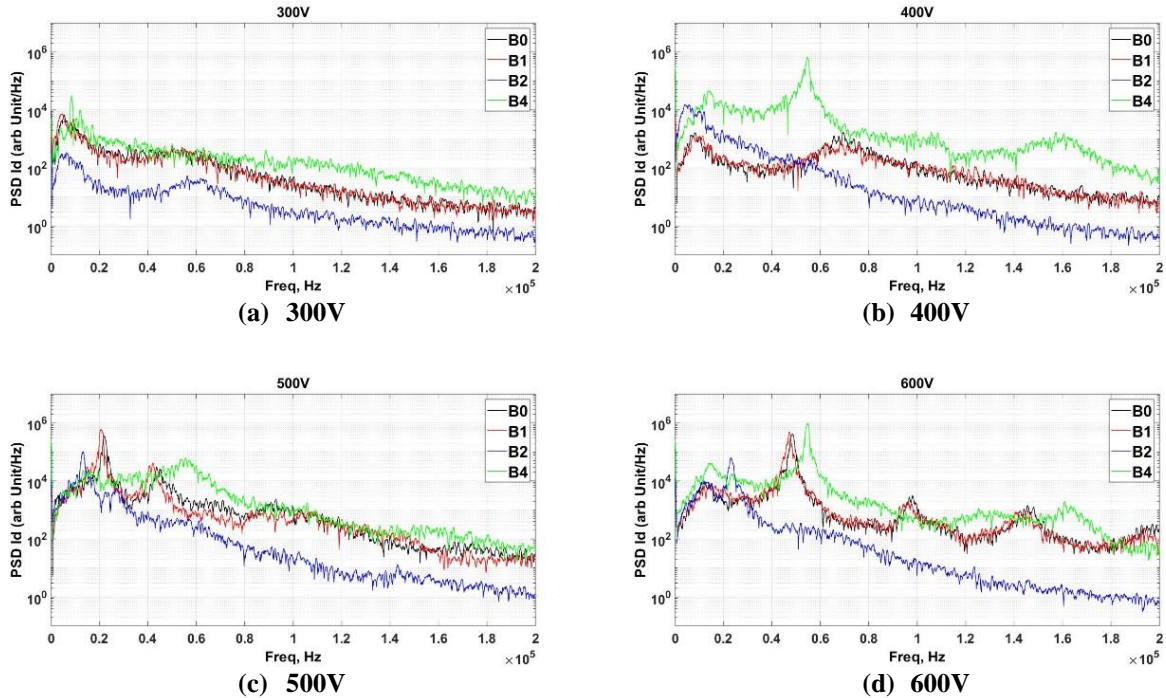


**Figure 15. The discharge current PSDs for the thruster operating at 20.8-A at discharge voltages of 300-V, 400-V, 500-V, and 600-V.**

Finally, Figures 16a-d present the IVB maps that were performed at an anode flow rate of 20.6-mg/s, discharge voltage range of 100-V to 610-V, and cathode flow fraction (CFF) of 7%. The IVB maps for configurations B0 and B1 are qualitatively and quantitatively very similar; they show that the thruster operated in a very quiescent mode until a discharge voltage of ~450-V was reached, then the thruster started mode hopping to a higher oscillatory mode and then fully transitioned to a high oscillatory mode. The IVB map for configuration B2 shows that the thruster transitioned to a higher oscillatory mode around 375-V; however, the thruster's oscillation levels at 500V and 600V were lower than the levels for configurations B0 and B1. Finally, the IVB map for configuration B4 shows that the thruster transitioned to a higher oscillatory mode at approximately 325-V, and the thruster oscillation levels were significantly higher than configurations B0, B1, and B2 above a discharge voltage of 325-V.

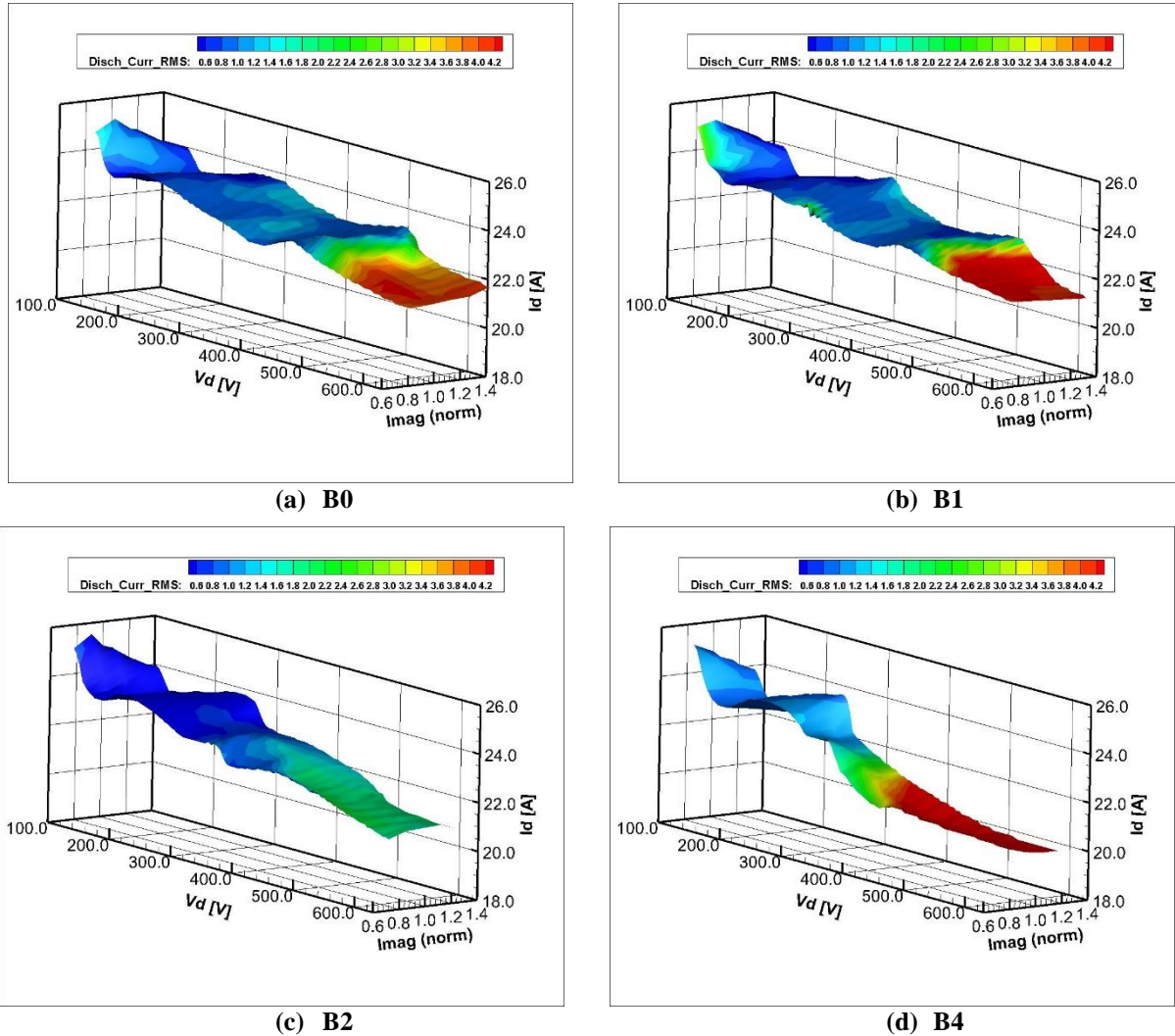


**Figure 16. Configuration B0, B1, B2, and B4 IVBs at 20.6-mg/s, CFF of 7%, and discharge voltage sweep from 100-V to 610-V. Note that for configuration B4, thruster operation at a normalized field setting of 0.75 was not performed due to the high oscillation levels.**

#### d. Body Current Profiles

All tests were performed in the thruster-cathode tied configuration. Figures 17a-d below present the body current collected by the thruster surfaces during the various tests. Figure 17a shows that at 300-V operation, all configurations had similar body current profiles with the B4 configuration collecting slightly higher current at normalized field strengths below 1 and lower current above a normalized field strengths above 1. Figure 17b shows that at 400-V, similar trends were observed for B0, B1, and B2; however, for configuration B4, significantly more current was being collected by the thruster at most magnetic field operating points. Figure 17c shows that at the 500-V operation configuration, B4's body current was also significantly higher than the other configurations, but B2 collected more current at the normalized field settings above 1. Figure 17d shows that at 600-V operation, configuration B4's body current was also significantly higher than the other configurations, but B2 collected less current at all the normalized field settings. Collected body current for configuration B4 for 400-V, 500-V, and 600-V operation was significantly higher than configurations B0, B1, and B2. Part of that increase can be attributed to the higher anode flow rates that were needed for configuration B4, and it could also be attributed to the increase in the oscillation levels of B4 configuration compared to B0, B1, and B2 at discharge voltages greater than 325-V.

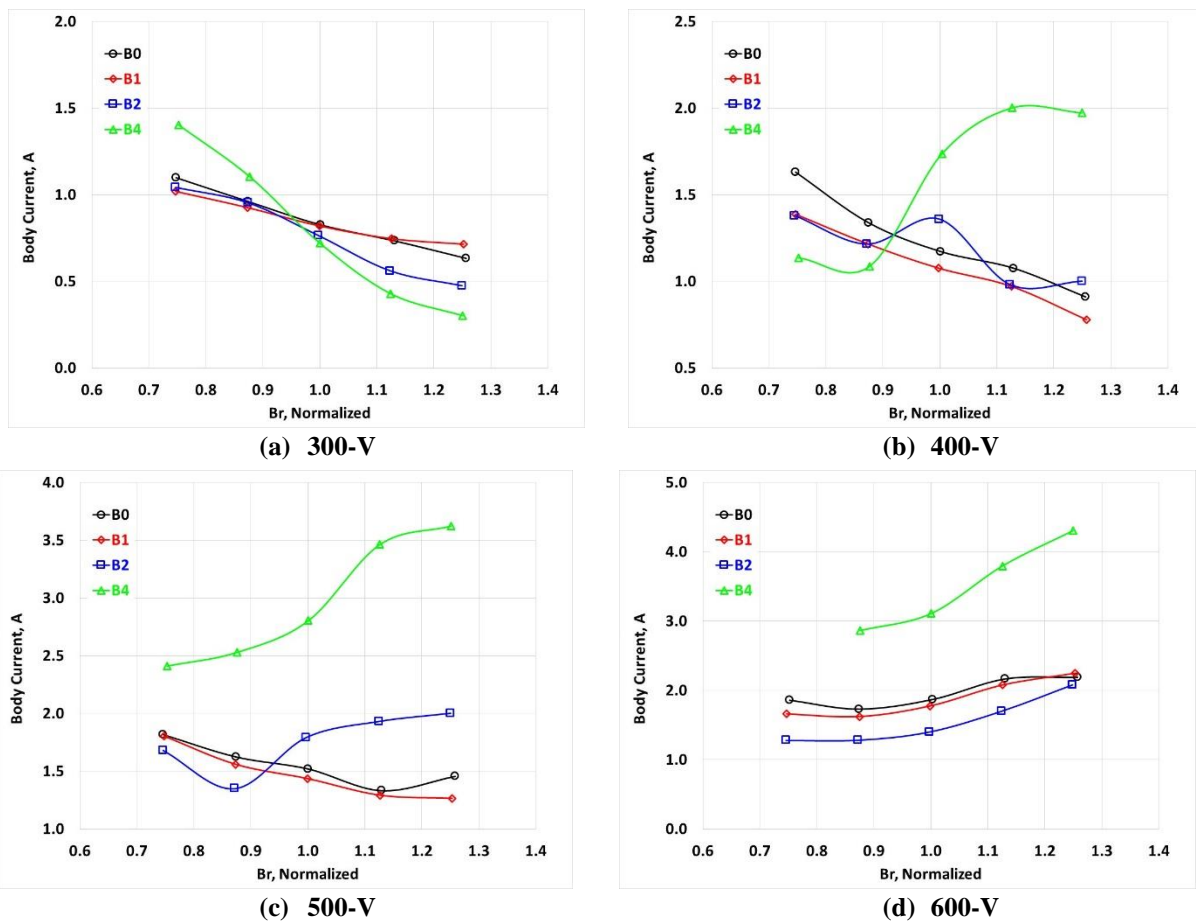


Figure 17. Configuration B0, B1, B2, and B4 body current profiles for 300-V, 400-V, 500-V, 600-V discharge voltage operation at 20.8-A.

### e. Wear Characterization

Thruster front pole cover and discharge chamber wear was characterized for configurations B0, B1, and B2. Configuration B0 characterization was performed to provide a reference wear rate (for the VF-6 test facility and TDU-1 thruster configuration) to compare against for configurations B1 and B2. No wear tests were performed for configuration B4 due to the high level of oscillations that were observed during configuration B4 characterization tests. For the wear tests of configurations B0, B1, and B2, the thruster was operated for approximately 250-hours at each configuration.

Similar to the approach taken in previous HERMeS wear tests, the inner front pole cover (IFPC) and outer front pole cover (OFPC) were modified in order to better characterize component erosion rates [25, 43]. Specifically, graphite masks were installed to provide unexposed surfaces to use as a reference for post-test analysis. The IFPC configuration used during this test is shown in Figure 18. The IFPC was made of graphite that was polished prior to installation in order to minimize the variation in pre-test surface roughness and thus provide as uniform a baseline surface as possible. Unlike in previous wear tests, the IFPC was re-polished prior to each wear test segment [25]. Two 0.5-mm-thick graphite masks were installed at the 12-o'clock and 6-o'clock locations of the IFPC. These masks are identical to the graphite masks used during previous TDU wear tests [23, 25].

The OFPC used during this study is also shown in Figure 18. The OFPC was made of graphite with various regions polished and masked prior to each test segment. For the B2 segment, the region between 12 and 2-o'clock was polished, and masks were placed at the 12, 2, and 8-o'clock positions. The 3 to 4-o'clock region of the OFPC was polished prior to the B1 segment, and masks were installed at the 3 and 4-o'clock positions. Finally, the region between 9 and 10-o'clock was polished prior to the B0 segment, and masks were placed at the 6, 9, and 10-o'clock locations. All reported OFPC erosion rates are from locations polished and masked prior to the start of each test segment. All erosion measurements were made with a chromatic, white-light non-contact benchtop profilometer. The employed profilometer is equipped with an optical pen oriented normal to the HET exit plane with a 3-mm measuring range. All acquired profilometry data were analyzed according to the guidance established in the ISO 5436-1 measurement standard for a type A1 step (i.e., a wide groove with a flat bottom). Uncertainty was quantified using the technique detailed by Mackey *et al* [44] that accounts for instrument error, surface roughness, wear due to operation at points other than the nominal wear point, and the non-flat nature of the acquired profiles. The results of this uncertainty analysis yielded typical uncertainties on the order of 10% of the measurement for this work. Note that detail scans of the discharge channel were made, and detailed analysis of those results are ongoing.

The OFPC used during this study is also shown in Figure 18. The OFPC was made of graphite with various regions polished and masked prior to each test segment. For the B2 segment, the region between 12 and 2-o'clock was polished, and masks were placed at the 12, 2, and 8-o'clock positions. The 3 to 4-o'clock region of the OFPC was polished prior to the B1 segment, and masks were installed at the 3 and 4-o'clock positions. Finally, the region between 9 and 10-o'clock was polished prior to the B0 segment, and masks were placed at the 6, 9, and 10-o'clock locations. All reported OFPC erosion rates are from locations polished and masked prior to the start of each test segment. All erosion measurements were made with a chromatic, white-light non-contact benchtop profilometer. The employed profilometer is equipped with an optical pen oriented normal to the HET exit plane with a 3-mm measuring range. All acquired profilometry data were analyzed according to the guidance established in the ISO 5436-1 measurement standard for a type A1 step (i.e., a wide groove with a flat bottom). Uncertainty was quantified using the technique detailed by Mackey *et al* [44] that accounts for instrument error, surface roughness, wear due to operation at points other than the nominal wear point, and the non-flat nature of the acquired profiles. The results of this uncertainty analysis yielded typical uncertainties on the order of 10% of the measurement for this work. Note that detail scans of the discharge channel were made, and detailed analysis of those results are ongoing.

#### 1. Wear Results: Inner Front Pole Cover

The IFPC erosion rates measured near the 12-o'clock mask are shown in Figure 19 for the B0, B1, and B2 configurations. The data have been normalized by the maximum erosion rate measured for the B0 configuration. In Figure 19, a normalized radius of 0 corresponds to the edge of the IFPC closest to the cathode whereas a radius of 1 corresponds to the edge closest to the discharge channel. The truncation of the long duration wear test (LDWT) data near the inner IFPC edge is due to the fact that the employed masks only covered approximately 95% of the IFPC. Near the center of the IFPC, the mask fastener interfered with the unexposed reference surface, thus precluding data analysis in this region.

Consistent with previous empirical and analytic results, the erosion rate measured during the MS Optimization Test minimized near the center of the IFPC, gradually increased towards the keeper and discharge channel, and showed azimuthal symmetry for all three magnetic field configurations [21, 23, 25]. Overall, the IFPC erosion rates varied as expected with the change in magnetic field topology. Specifically, the erosion rates of B1 were approximately 65% of the rates for B0, and the erosion rates for B2 were 40% of the rates for B0.

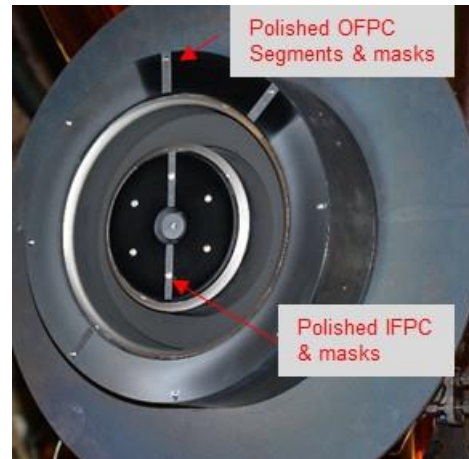


**Figure 18. Pole cover configuration for the B2 segment of the MS Optimization Test.**

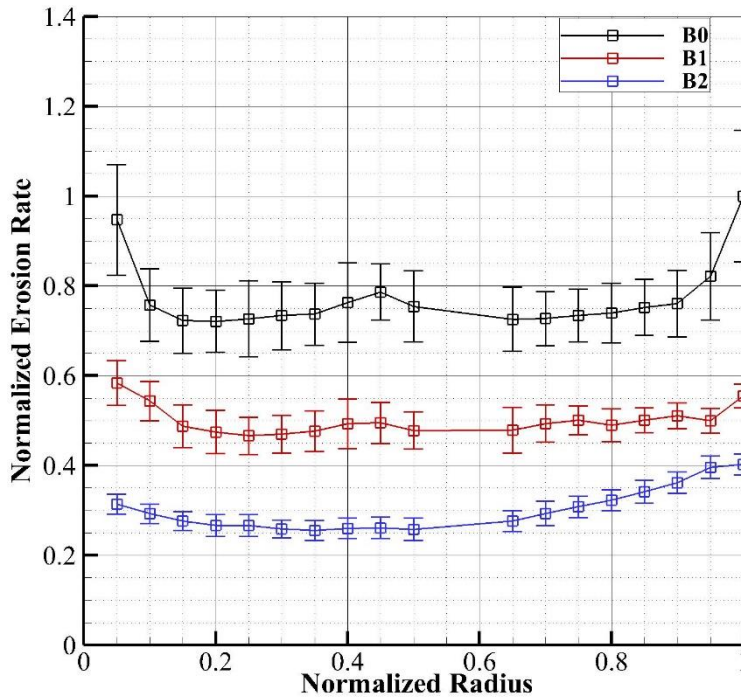


**Figure 19. IFPC erosion rates measured for the B0, B1, and B2 configurations.**

*2. Wear Results: Outer Front Pole Cover*

Figure 20 shows the OFPC erosion rates measured as a function of normalized OFPC radius for the B1 and B2 configurations. The data have been normalized by the maximum erosion rate measured for the B1 configuration. In Figure 20, a normalized radius of 0 corresponds to the edge of the OFPC closest to the discharge channel whereas a radius of 1 corresponds to the outer edge of the thruster. The truncation of the data near the inner edge is due to the fact that the employed masks do not cover the entire width of the OFPC. Near the outer edge, the mask fastener interfered with the unexposed reference surface, thus precluding data analysis in this region. Data from the B0 configuration is omitted as the shorter operating time for that segment yielded large uncertainties for those measurements but the rates were below those measured for B1 and B2.

Consistent with IFPC measurements, the OFPC erosion rates decreased by an average of 31% for B2 relative to B1. However, unlike with the IFPC, this decrease is within the uncertainty of the measurement. Nevertheless, taken together, the wear results strongly suggest that the change in magnetic field topology had the intended effect of lowering the net erosion rate of the pole covers for the 600-V, 12.5-kW operating condition.

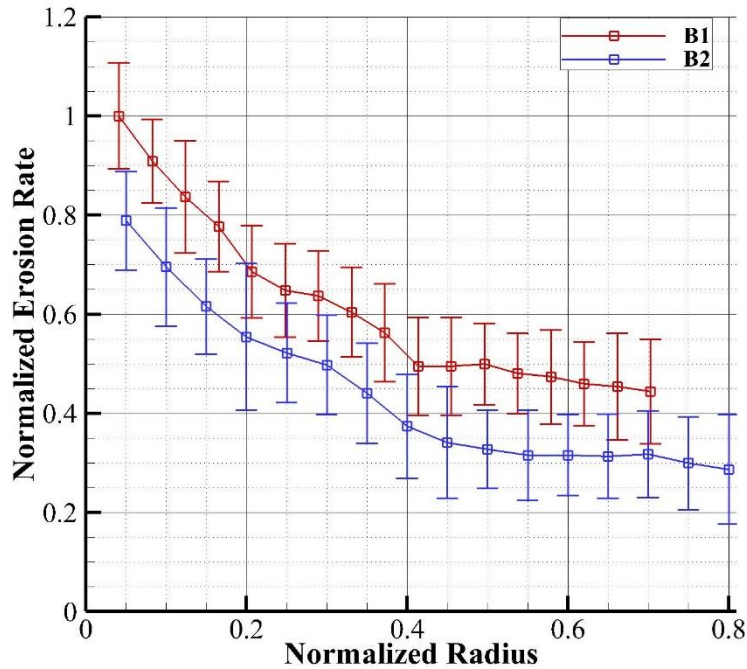


Figure 20. OFPC erosion rates measured for the B1 and B2 configurations.

## VI. Discussion of Results

Table 2 below presents a summary of the TDU-1 performance and discharge current ripple data for configurations B0, B1, B2, and B4 for the various thruster operating discharge voltages at the normalized magnetic field setting of 1.

Table 2. Configurations B0, B1, B2, and B4 thrust efficiency, specific impulse, anode flow rate (mg/s), and Id p2p % at a discharge current of 20.8-A and discharge voltage of 300 V, 400 V, 500 V, and 600 V at a normalized magnetic field setting of 1.

Config	300-V				400-V				500-V				600-V			
	$\eta$	Isp, sec	Ma, mg/s	Id p2p %	$\eta$	Isp, sec	Ma	Id p2p %	$\eta$	Isp, sec	M, mg/s	Id p2p %	$\eta$	Isp, sec	Ma, mg/s	Id p2p %
B0	.61	2010	18.52	37	.66	2372	19.15	31	.67	2662	19.50	82	.69	2903	20.13	92
B1	.59	1965	18.76	39	.64	2335	19.13	28	.65	2606	19.48	92	.66	2838	20.04	85
B2	.61	1973	19.09	11	.63	2286	19.36	55	.65	2378	19.72	92	.67	2836	20.36	43
B4	.61	1965	19.20	58	.64	2259	20.42	111	.63	2475	20.90	131	.65	2755	20.90	225

The data presented in Table 2 for the most part are representative of the general trends that were observed during the testing of configurations B0, B1, B2, and B4. A number of trends can be inferred from Table 2:

- For all configurations, the thruster performance increased with discharge power;
- For all configurations, higher anode flow rates were required as the discharge voltage was increased to maintain a discharge current of 20.8-A; this is typical of Hall thrusters and has been well documented with the B0 configuration;
- For a given discharge voltage, higher flow rates were required to attain a discharge current of 20.8-A as we transitioned from configuration B0 to B1 to B2 and to B4. As the ionization and acceleration zones retracted into the discharge chamber (moved upstream as is shown in Figs. 9 and 10) the ionization efficiency varied and more neutral xenon flow was required to achieve the same beam current as we transitioned from

configuration B0 to B4. Similar trends were observed during the H6US/H6MS [28, 45] and 300M/300MS [27, 46] where higher doubly and triply ionized Xe was measured in the plume of the magnetically shielded version of both the H6 and 300M thrusters. Analysis of the plasma probe data that was collected during this test campaign will help further elucidate and provide insights into what was driving this variation; and

- The discharge current ripple and IVB maps for configurations B0 and B1 were almost identical. Configuration B2 discharge current information indicated the lowest p2p but the thruster mode hopped to a higher oscillatory mode at a discharge voltage of ~400-V instead of configuration B0 and B1 of ~450-V. The discharge current p2p at 500-V for configurations B0, B1, and B2 were similar but configuration B2 discharge current p2p at 600-V were almost 50% of the levels found during configuration B0 and B1 tests. Configuration B4 discharge current ripple may indicate that as the ionization zone was further moved upstream and the interaction with the discharge channel walls increased that resulted in a noticeable shift in the discharge characteristics as evident but the ripple data for configuration B4.

In summary, the analyzed test results along with the Hall2De simulations that were performed during the Phase I study, indicate that the B1 configuration was very similar to the B0 configuration and for the most part the magnetic shielding was preserved. However, as we transitioned to B2 and B4, onset of unshielding occurred with B2 and progressed more with B4.

To further our understanding of various trends observed during this campaign, analysis of the following test results is ongoing:

- Plasma probe sweeps for configurations B0-B4 at discharge voltages of 300-V and 600-V. This includes probe sweeps with the Faraday probe, RPA, Wien filter, and Langmuir probe. Understanding the plume divergence and ionization state of the ion beam will provide invaluable insights;
- Temperature data of various thruster components including the discharge channel. The thermocouple data will, especially on the discharge channel walls provide additional guidance to the Hall2De simulations in better predicting the discharge location; and
- Cathode flow fraction test data that includes performance and stability results.

## VII. Conclusions, Summary, And Future Work

Extensive testing of the HERMeS thrusters (TDU-1, TDU-2, and TDU-3) has been performed at NASA GRC and JPL. Modeling and test results to date, indicate that the thruster design meets the 23-krh life service capability with a 50% margin. However, in order to further refine the design, the NASA GRC and JPL team explored performing modifications to the thruster magnetic field topology to reduce the front pole cover erosion rates, reduce plume divergence, improve thruster stability, and improve its magnetic circuit performance.

Four new magnetic field topologies were designed at NASA GRC and they were numerically modeled by NASA JPL with Hall2De. Modeling of the four candidate magnetic field topologies found that, as expected, the discharge channel erosion rates in going from B0 to B4 rise, with increasing values occurring further upstream from the channel exit along the chamfer. Though the rates increase it is noted that the highest values observed in B4 remain approximately two orders of magnitude below those observed in the H6US. Moreover, at the maximum value of ~100- $\mu\text{m}/\text{kh}$  (B4) it would take approximately 38-krh for the channel to be completely eroded (assuming that the rate does not change as material is lost during thruster operation). New magnetic circuit components were manufactured, installed, and the magnetic field topologies (B0, B1, B2, and B4) were measured along discharge channel centerline and 2D map. The measured magnetic topologies were found to very closely match the designed magnetic field topologies.

In Phase I, LIF measurements were performed for the three candidate topologies. LIF measurements along the discharge chamber centerline found that upstream retraction of the peak magnetic field does result in an upstream shift of the acceleration zone but the magnitude of the extension does not correspond one-to-one to the shift in the location of the peak magnetic field magnitude.

In Phase II, performance, stability, and wear characterization tests were performed for configurations B0, B1, B2, and B4 (no wear). Performance characterization test results found that, in general, the thruster performance for all configurations was very similar with configuration B0 still demonstrating the highest performance. Stability characterization test results found that configurations B0 and B1 were very similar, configuration B2 had a lower discharge current ripple than B0 and B1 but mode hopped to a higher oscillatory mode at a lower discharge voltage than B0 and B1, and configuration B4 had very large oscillations for discharge voltages of above 400-V. At

12.5kW/600-V operation, the inner front pole cover erosion rates for configuration B1 were approximately 65% relative to B0, and the erosion rates for configuration B2 were 40% relative to B0.

Analysis of the performance, stability, and wear test results of configurations B0, B1, B2, and B4 indicates that configuration B2 may present an alternative option for B0 because it mostly maintained the same performance and stability as configuration B0 but with 40% of the inner front pole cover erosion rate.

Future work will include analysis of the plasma probe array data to determine if the thruster plume divergence changed due to changes in the magnetic field topology. Additional modeling with the Hall2De code will also be performed to help elucidate trends observed during this test campaign.

### Appendix A

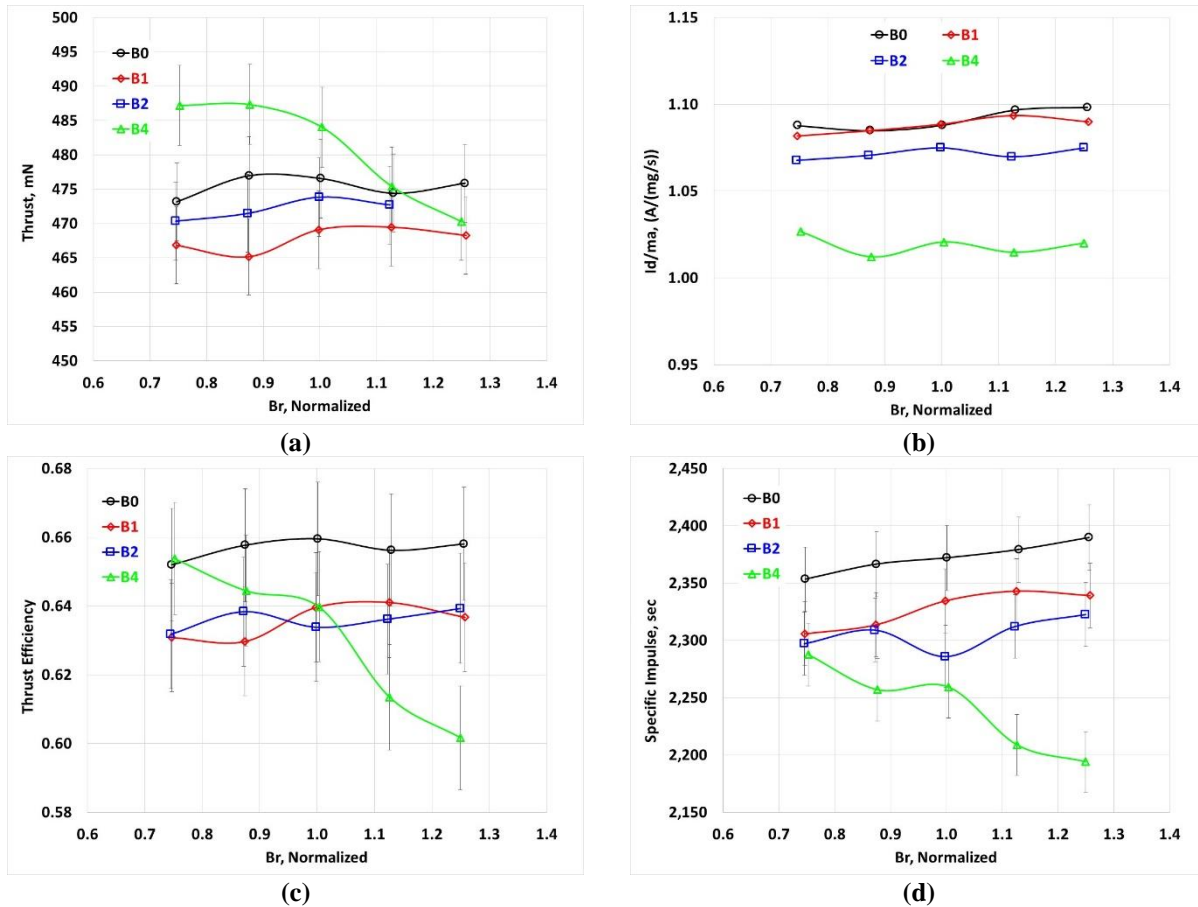
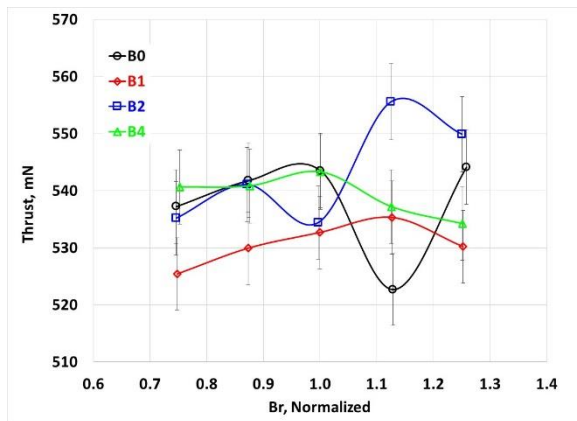
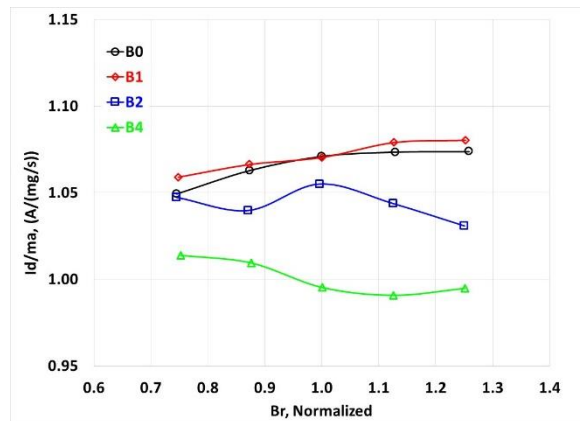


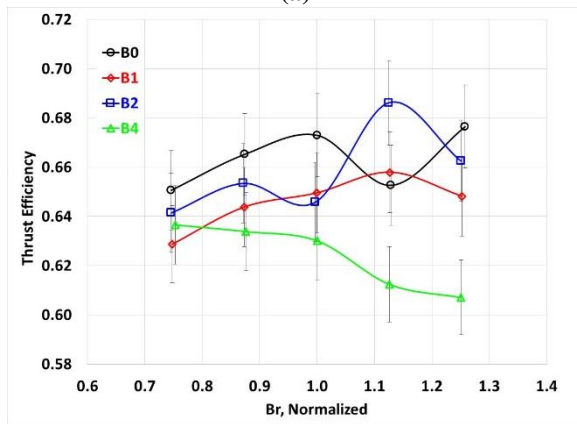
Figure 21 a-d. Trends of thrust,  $I_d/m_a$ , thrust efficiency, and specific impulse variation with normalized magnetic field setting for configurations B0, B1, B2, and B4 for the thruster operation at 8.33-kW and 400-V discharge voltage.



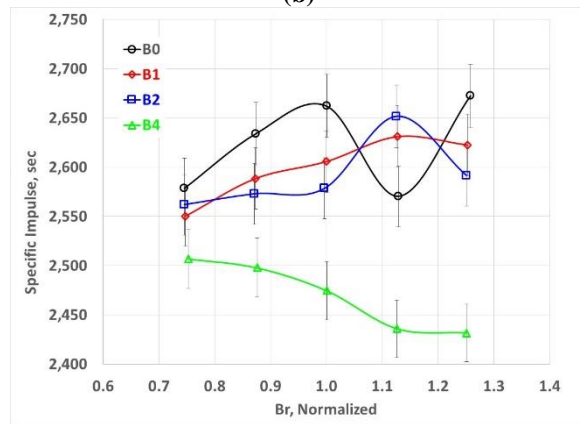
(a)



(b)



(c)



(d)

Figure 22 a-d. Trends of thrust,  $I_d/m_a$ , thrust efficiency, and specific impulse variation with normalized magnetic field setting for configurations B0, B1, B2, and B4 for the thruster operation at 10.4-kW and 500-V discharge voltage.

## Acknowledgments

The authors would like to like to thank the Space Technology Mission Directorate through the Solar Electric Propulsion Technology Demonstration Mission Project for funding the joint NASA GRC and JPL development of the Advanced Electric Propulsion System. The authors would also like to thank the many NASA/Aerojet review board members and subject matter experts for providing their expertise and technical guidance to the development of AEPS and its broader Ion Propulsion Subsystem mission application.

## References

- 
- [1] Smith, B. K., Nazario, M. L., and Cunningham, C. C. "Solar Electric Propulsion Vehicle Demonstration to Support Future Space Exploration Missions," Space Propulsion 2012. Bordeaux, France, 2012.
  - [2] Free, J. "Architecture Status," *NASA Advisory Council Human Exploration and Operations Committee Meeting*. Washington, DC, 2017.
  - [3] Congress, t. "National Aeronautics and Space Administration Transition Authorization Act of 2017." 2017.
  - [4] Leiter, H., Kukies, R., Killinger, R., Bonelli, E., Scaranzin, S., Scortecci, F., Neumann, H., and Tartz, M. "RIT-22 Ion Propulsion System: 5,000h Endurance Test Results and Life Prediction." Cincinnati, OH, 2007.
  - [5] NASA. (2019). NASA Awards Artemis Contract for Lunar Gateway Power, Propulsion Available: <https://www.nasa.gov/press-release/nasa-awards-artemis-contract-for-lunar-gateway-power-propulsion>
  - [5] Gerstenmaier, W. "Progress in Defining the Deep Space Gateway and Transport Plan," *NASA Advisory Council Human Exploration and Operations Committee Meeting*, 2017
  - [7] Jackson, J., et al. "13kW Advanced Electric Propulsion Flight System Development and Qualification," IEPC-2017-223, *35th International Electric Propulsion Conference*. ERPS, Atlanta, GA, 2017.
  - [8] Peterson, P., Herman, D., Kamhawi, H., Frieman, D., Huang, W., Verhey, T., Dinca, D., Boomer, K., Pinero, L., Criswell, K., Hall, S., Birchenough, A., Gilland, J., Hofer, R., Polk, J., Lobbia, R., Garner, C., and Kowalkowski, "Overview of NASA's Solar Electric Propulsion Project," IEPC-2019-836, presented in *36th International Electric Propulsion Conference*. ERPS, Vienna, Austria Sept. 2019.
  - [9] Hofer, R. R., and Kamhawi, H. "Development Status of a 12.5 kW Hall Thruster for the Asteroid Redirect Robotic Mission," *35th International Electric Propulsion Conference*. ERPS, Atlanta, GA, 2017.
  - [10] Hofer, R., Lobbia, R., Chaplin, V., Ortega, A., Mikellides, I., Polk, J., Kamhawi, H., Frieman, J., Huang, W., Peterson, P., and Herman, D., "Completing the Development of the 12.5 kW Hall Effect Rocket with Magnetic Shielding (HERMeS)," IEPC-2019-193, presented in *36th International Electric Propulsion Conference*. ERPS, Vienna, Austria Sept. 2019.
  - [11] Kamhawi, H., Huang, W., Haag, T. W., Yim, J., Chang, L., Clayman, L., Herman, D. A., Shastry, R., Thomas, R., Griffith, C., Myers, J., Williams, G. J., Mikellides, I., Hofer, R. R., Polk, J. E., and Goebel, D. M. "Overview of the Development of the Solar Electric Propulsion Technology Demonstration Mission 12.5-kW Hall Thruster," *50th AIAA/ASME/SAE/ASEE Joint Propulsion Conference*. Cleveland, OH, 2014.
  - [12] Kamhawi, H., Haag, T., Huang, W., Herman, D. A., Thomas, R., Shastry, R., Yim, J., Chang, L., Clayman, L., Verhey, T., Griffiths, C., Myers, J., Williams, G., Mikellides, I. G., Hofer, R. R., Polk, J. E., and Jorns, B. A. "Performance Characterization of the Solar Electric Propulsion Technology Demonstration Mission 12.5-kW Hall Thruster," *34th International Electric Propulsion Conference*. Kobe, Japan, 2015.
  - [13] Hofer, R. R., Kamhawi, H., Herman, D. A., Polk, J. E., Snyder, J. S., Mikellides, I., Huang, W., Myers, J., Yim, J., Williams, G. J., Lopez Ortega, A., Jorns, B., Sekerak, M., Griffiths, C., Shastry, R., Haag, T. W., Verhey, T. R., Gilliam, B., Katz, I., Goebel, D. M., Anderson, J. R., Gilland, J. H., and Clayman, L. "Development Approach and Status of the 12.5 kW HERMeS Hall Thruster for the Solar Electric Propulsion Technology Demonstration Mission," *30th International Electric Propulsion Conference*. Kobe, Hyogo, Japan, 2015.
  - [14] Myers, J., Kamhawi, H., and Yim, J. "HERMeS Thermal Model," *51st Joint Propulsion Conference*. Orlando, FL, 2015.
  - [15] Williams, G. J., and Kamhawi, H. "Optical characterization of component wear and near-field plasma of the HERMeS thruster," *62nd JANNAF Propulsion Meeting*. Nashville, TN, 2015.
  - [16] Kamhawi, H., Haag, T. W., Huang, W., Herman, D. A., Williams, G. J., Peterson, P. Y., Hofer, R. R., and Mikellides, I. "Performance, Stability, and Pressure Effects Characterization Tests of NASA's 12.5-kW Hall Effect Rocket with Magnetic Shielding (HERMeS) Thruster," *AIAA\_2016-482652nd AIAA/SAE/ASEE Joint Propulsion Conference*. Salt Lake City, UT, 2016.

- 
- [17] Peterson, P. Y., Kamhawi, H., Huang, W., Williams, G., Gilland, J., Yim, J., Hofer, R. R., and Herman, D. "NASA's HERMeS Hall Thruster Electrical Configuration Characterization," AIAA-2016-5027 *52nd AIAA/ASME/SAE/ASEE Joint Propulsion Conference*. AIAA, Salt Lake City, UT, 2016.
- [18] Huang, W., Kamhawi, H., and Haag, T. W. "Facility Effect Characterization Test of NASA's HERMeS Hall Thruster," *52nd AIAA/SAE/ASEE Joint Propulsion Conference*. Salt Lake City, UT, 2016.
- [19] Huang, W., Kamhawi, H., and Haag, T. W. "Plasma Oscillation Characterization of NASA's HERMeS Hall Thruster via High Speed Imaging," *52nd AIAA/SAE/ASEE Joint Propulsion Conference*. Salt Lake City, UT, 2016.
- [20] Hofer, R. R., and Kamhawi, H. "Development Status of the 12.5 kW HERMeS Hall Thruster Solar Electric Propulsion Technology Demonstration Mission," *52nd AIAA/SAE/ASEE Joint Propulsion Conference*. Salt Lake City, UT, 2016.
- [21] Williams, G. J., Gilland, J. H., Peterson, P. Y., Kamhawi, H., Huang, W., Swiatek, M., Joppeck, C., Yim, J., and Haag, T. W. "Wear Testing of the HERMeS Thruster," AIAA-2016-4645, *52nd AIAA/SAE/ASEE Joint Propulsion Conference*. Salt Lake City, UT, 2016.
- [22] Kamhawi, H., Huang, W., Gilland, J., Mackey, J., Yim, J., Pinero, L., Williams, G., Peterson, P., and Herman, D., "Performance, Stability, and Plume Characterization of the HERMeS Thruster with Boron Nitride Silica Composite Discharge Channel" in *IEPC-2017-392*.
- [23] G. Williams, J. H. Gilland, H. Kamhawi, M. Choi, P. Y. Peterson, and D. A. Herman, "Wear Trends of the HERMeS Thruster as a Function of Throttle Point," IEPC Paper 2017-207, presented at the 35th International Electric Propulsion Conference, Atlanta, GA, 2017.
- [24] P. Peterson, J. Frieman, H. Kamhawi, G. Williams, D. Herman, J. Gilland, and R. Hofer, "NASA Hermes Hall Thruster Long Duration Wear Test," in *65th JANNAF Propulsion Meeting*, Long Beach, CA, 2018.
- [25] Frieman, J., Kamhawi, H., Williams, G., Herman, D., Peterson, P., Gilland, J., and Hofer, H., "Long Duration Wear Test of the NASA HERMeS Thruster," AIAA-2018-4645, AIAA Propulsion and Energy Forum, Cincinnati, OH, Jul 9-11, 2018.
- [26] De Grys, K., Mathers, A., Welander, B., and Khayms, V., "Demonstration of 10,400 Hours of Operation on 4.5 kW Qualification Model Hall Thruster", 46th AIAA/ASME/SAE/ASEE Joint Propulsion Conference & Exhibit, Joint Propulsion Conferences
- [27] Kamhawi, H., et al., "Performance and Thermal Characterization of the 20 kW 300MS Hall Effect Thruster", *33rd International Electric Propulsion Conference*, 2013-444, Washington, DC, 6-10 Oct., 2013.
- [28] R. R. Hofer, D. M. Goebel, I. G. Mikellides, and I. Katz, "Magnetic shielding of a laboratory Hall thruster. Phase II. Experiments," *Journal of Applied Physics*, vol. 115, no. 4, Jan 28, 2014.
- [29] R. Shastry, W. Huang, and H. Kamhawi, "Near-Surface Plasma Characterization of the 12.5-kW NASA TDU1 Hall Thruster," AIAA-2015-3919, presented in *51st Joint Propulsion Conference*, ed. Orlando, FL, 2015.
- [30] I. G. Mikellides, I. Katz, R. R. Hofer, and D. M. Goebel, "Magnetic shielding of a laboratory Hall thruster. I. Theory and validation," *Journal of Applied Physics*, vol. 115, no. 4, Jan 28, 2014.
- [31] I. G. Mikellides, I. Katz, R. R. Hofer, and D. M. Goebel, "Magnetic shielding of walls from the unmagnetized ion beam in a Hall thruster," *Applied Physics Letters*, vol. 102, no. 2, Jan 14, 2013.
- [32] Kamhawi, H., Huang, W., and Mikellides, I., "Optimization of the Magnetic Field Topology of the Hall Effect Rocket with Magnetic Shielding," AIAA-2018-4720, AIAA Propulsion and Energy Forum, Cincinnati, OH, Jul 9-11, 2018.
- [33] Huang, W., Kamhawi, H. and Herman, D., "Ion Velocity in the Discharge Channel and Near-Field of the HERMeS Hall Thruster," AIAA-2018-4723, AIAA Propulsion and Energy Forum, Cincinnati, OH, Jul 9-11, 2018.
- [34] Huang, W., Kamhawi, H., and Herman, D., "Variation in Ion Acceleration Characteristics of the HERMeS Hall Thruster during Magnetic Optimization," presented at the 36<sup>th</sup> International Electric Propulsion Conference, IEPC-2019-713, Vienna, Austria, 2019.
- [35] Gray, T., Williams, G., Kamhawi, H., Frieman, J., "Non-intrusive Characterization of the Wear of the HERMeS Thruster Using Optical Emission Spectroscopy," presented at the 36<sup>th</sup> International Electric Propulsion Conference, IEPC-2019-841, Vienna, Austria, 2019.
- [36] Patterson, M. J., and Sovey, J. S. "History of Electric Propulsion at NASA Glenn Research Center: 1956 to Present," *Journal of Aerospace Engineering* Vol. 26, No. 2, 2013, pp. 300-316.
- [37] P. Y. Peterson, H. Kamhawi, W. Huang, J. Yim, T. W. Haag, J. Mackey, M. McVetta, L. Sorrelle, T. Tomsik, R. Gilligan, and D. Herman, "Reconfiguration of NASA GRC's Vacuum Facility 6 for Testing of Advanced Electric Propulsion System (AEPS) Hardware," presented at the 35<sup>th</sup> International Electric Propulsion Conference, IEPC-2017-028, Atlanta, GA, 2017.

- 
- [38] I. Mikellides, I. Katz, R. Hofer, D. Goebel, K. de Grys, and A. Mathers, "Magnetic Shielding of the Acceleration Channel Walls in a Long-Life Hall Thruster," presented in *Joint Propulsion Conference, AIAA-10-6942*, Nashville, Tennessee 2010.
- [39] I. Mikellides, R. R. Hofer, I. Katz, and D. M. Goebel, "Magnetic Shielding of Hall Thrusters at High Discharge Voltages," *Journal of Applied Physics*, vol. 116, 2013.
- [40] R. R. Hofer, H. Kamhawi, I. Mikellides, D. A. Herman, J. E. Polk, W. Huang, *et al.*, "Design Methodology and Scaling of the 12.5 kW HERMeS Hall Thruster for the Solar Electric Propulsion Technology Demonstration Mission," presented at the Presented at the 62nd JANNAP Propulsion Meeting, Nashville, TN, 2015.
- [41] T. W. Haag, "Thrust stand for high-power electric propulsion devices," *Review of Scientific Instruments*, vol. 62, 1991 1991.
- [42] T. W. Haag and M. Osborn, "RHETT/EPDM performance characterization," in *International Electric Propulsion Conference, IEPC-97-107*, Cleveland, OH, 1997.
- [43] Frieman, J., Kamhawi, H., Peterson, P., Herman, D., Gilland, J, and Hofer, H., "Impact of Facility Pressure on the Wear of the HERMeS Hall Thruster," IEPC-2019-714, presented in *36th International Electric Propulsion Conference*. ERPS, Vienna, Austria Sept. 2019.
- [44] Mackey, J., Frieman, J. D., Ahern, D. M., and Gilland, J. H., "Uncertainty in Electric Propulsion Erosion Measurements," AIAA\_2019-3896, *2019 AIAA Joint Propulsion Conference*, 2019, Indianapolis, IN, August 2019.
- [45] Hofer, H, Goebel, D., Mikellides, I., Katz, I., "Design of a Laboratory Hall Thruster with Magnetically Shielded Channel Walls, Phase II Experiments," AIAA-2012-3788, AIAA Joint Propulsion Conference, Atlanta, GA, 2010.
- [46] Huang, W., Shastry, R., Soulas, G, Kamhawi, H., "Farfield Plume Measurements and Analysis on the NASA-300M and NASA-300-MS", *33rd International Electric Propulsion Conference*, 2013-444, Washington, DC, 6-10 Oct., 2013.IEPC-2013-057.